

⁵¹V NMR chemical shifts calculated from QM/MM models of Peroxo-forms of Vanadium Haloperoxidases.

K. R. Geethalakshmi,^[a] Mark P. Waller,^[a] Walter Thiel,^[a] Michael Bühl*^[b]

Abstract

QM/MM models of the peroxo-forms of vanadium containing haloperoxidases (VHPOs) are critically assessed in terms of active site geometries, hydrogen bonds within the active site, isotropic and anisotropic ⁵¹V NMR chemical shifts and TD-DFT excitation energies. The geometric stability within the active site of the protein is comparable to the respective native-forms, as indicated by low standard deviations in bond lengths across a number of local minima sampled along MD trajectories. There is a significant calculated upfield shift in $\delta(^{51}\text{V})$ upon formation of the peroxo from the respective native forms for both the vanadium containing chloroperoxidase (VCPO) and vanadium containing bromoperoxidase (VBPO) models, which is in qualitative agreement with ⁵¹V NMR experiments of VBPO in solution. The models show appreciable differences between the anisotropic chemical shifts of the different protonation states of the peroxo-form of VHPO. The most likely candidates for the peroxo-forms of the VHPO enzymes appear to be unprotonated or have a single proton on either of the equatorial oxygen ligands, based on QM/MM modeling in combination with X-ray, ⁵¹V NMR and UV-Vis data.

Keywords: Haloperoxidases, QM/MM, Anisotropic chemical shifts, DFT.

[a] K. R. Geethalakshmi, Dr. Mark P. Waller, Prof. Walter Thiel
Max-Planck-Institut für Kohlenforschung
Kaiser-Wilhelm-Platz 1, D-45470 Mülheim an der Ruhr, (Germany)

[b] Prof. Michael Bühl
School of Chemistry,
North Haugh, University of St. Andrews,
St. Andrews, Fife KY16 9ST, UK
E-mail: buehl@st-andrews.ac.uk
Fax: +(44)(0)1334 463808

Introduction

Vanadium peroxides have the potential to generate a number of biological and biochemical responses¹, and are utilized as insulin-mimetic agents in the treatment of human diabetes.² Vanadate is an essential prosthetic group of some isolated haloperoxidase enzymes.^{3,4,5,6} Two such important proteins within this family are vanadium containing chloroperoxidase (VCPO) and vanadium containing bromoperoxidase (VBPO). These enzymes use hydrogen peroxide to catalyze two-electron oxidations of a diverse range of substrates; for example, halide ions are oxidized to their corresponding hypohalous acids.⁷

According to protein X-ray crystallography, the native-form of VCPO⁸ shows the vanadate (protonated VO_4^{3-}) ligated by a single protein donor ligand, namely HIS496, affording a trigonal bipyramidal geometry. The apical hydroxo (or water) unit, O_4 , is hydrogen-bonded to a histidine residue (HIS404) in the native-form of VCPO, see Figure 1a. A similar bond pattern is found in the related VBPO, where this residue is labeled HIS416. The X-ray-derived structure of the peroxide-form of VCPO (2.24 Å resolution),⁸ denoted *p*-VCPO reveals a distorted tetragonal bipyramidal vanadium site, see Figure 1b. The peroxide ligand is coordinated in a side-on manner, and the apical oxygen ligand is no longer present. In addition to the two peroxo oxygen atoms bound to vanadium, two equatorial oxo ligands and a nitrogen ($\text{N}^{\text{E}2}$) from HIS496 in a pseudo-axial position complete the coordination scheme. One of the peroxo oxygens O_4 , is in a pseudo-axial position, and the other is in an equatorial position, therefore giving an overall distorted pyramidal coordination geometry. One of the equatorial oxo ligands is hydrogen bonded to ARG490, the coordinated peroxide is hydrogen bonded to the neighboring glycine amide backbone and also to LYS353, and the remaining oxo ligand is hydrogen bonded to ARG360, see Figure 1. It has been shown that the VCPO protein has a higher affinity for peroxovanadate than for vanadate.⁹

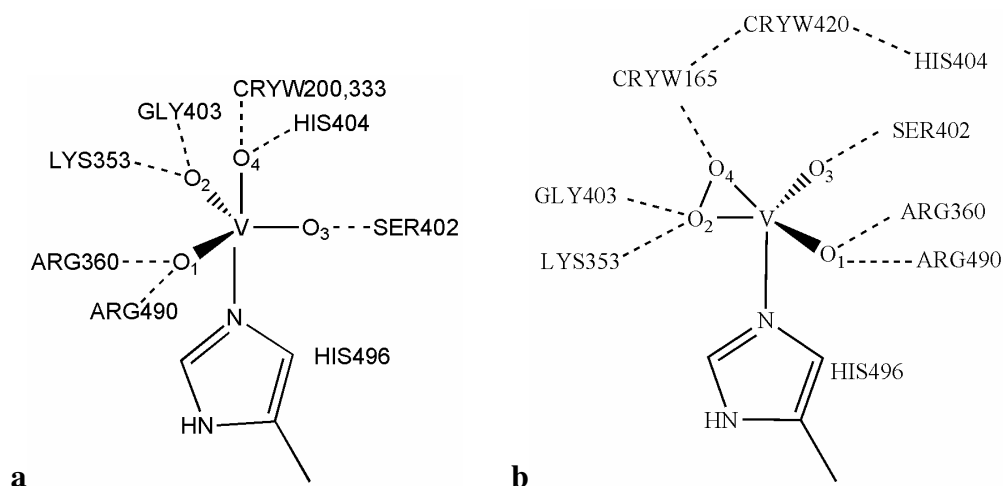
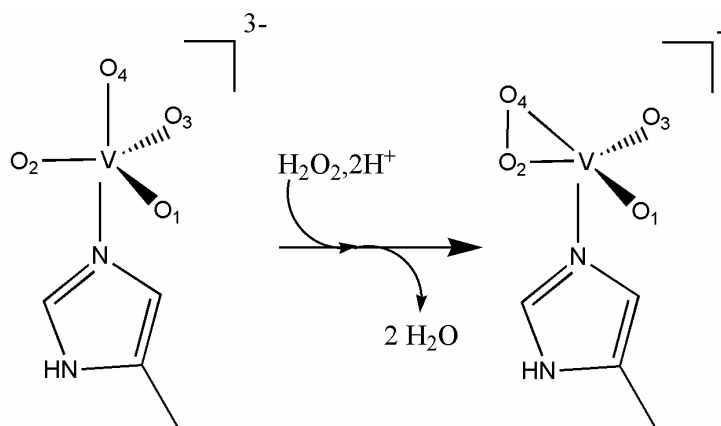


Figure 1. a. Vanadate moiety and coordinated imidazole in native VCPO. **b.** Peroxovanadate moiety and coordinated imidazole. The labels used throughout this study for potential hydrogen bonding interactions with the protein environment are consistent with those in the 1IDU.pdb file. The oxygen labeling scheme of the vanadate has been edited to be consistent with the *p*-VCPO labeling scheme within the 1IDU.pdb file.

A possible pathway for the formation of *p*-VCPO from VCPO has been outlined by Zampella et al.:¹⁰ Assuming the axial ligand in native VCPO (O₄ in Figure 1a) is present as OH⁻, which is made more basic by its H-bond to HIS404, this OH⁻ unit would deprotonate the approaching H₂O₂, thereby generating a HOO⁻ species. The weakly ligated axial water molecule dissociates from the vanadate and a side-on bound peroxide intermediate is formed after the departure of another water molecule, see Scheme 1. Furthermore, Zampella et al.¹⁰ suggested that an attack of a chloride ion on one of the peroxo atoms, and the uptake of a proton from one of the surrounding water molecules, leads to the generation of the hypochlorous acid (HOCl) and the restoration of the native state. Wever et al.¹¹ have shown that the vanadium ion plays the role of a strong Lewis acid which activates the peroxide, as seen by its inability to undergo redox cycling during catalysis. Kinetic studies showed that the protonation of the bound peroxo group is a crucial step in the heterolytic cleavage of the O-O bond.¹² These observations prompted the proposal of the protonated oxygen being transferred to the halide according to an oxo-transfer mechanism. A subsequent computational study disagrees,¹³ instead suggesting that the non-protonated peroxo oxygen is the atom transferred to the substrate.



Scheme 1. Proposed formation of VHPOs. The actual protonation states of vanadate and peroxovanadate moieties are not known with certainty.

The protonation state of the peroxovanadate cofactor affects its reactivity and this might be a crucial factor in tuning the selectivity profile of these enzymes.^{14,15}

Determining the protonation state of the intermediate peroxo-forms of the VHPO enzymes is experimentally challenging, as a VHPO enzyme shuttles between a trigonal bipyramidal structure (native-form) and a distorted tetragonal structure (peroxo-intermediate) during the catalytic cycle. The X-ray structure solved by Messerschmidt et al.⁸ failed to resolve the protonation state of the peroxovanadate active site within *p*-VCPO. Furthermore, there currently exists no X-ray crystal structure for the peroxo-form of VBPO (hereafter labeled *p*-VBPO). A gas-phase DFT study on the active site of VCPO¹³ addressed the protonation state of the intermediate peroxo-form of the enzyme, suggesting a singly protonated species. Protonation of the peroxovanadate was previously suggested¹⁶ to be a possible explanation for the difference between VCPO and VBPO, therefore further studies that incorporate the intrinsic environmental differences might be necessary.

Wever et al.⁹ used stopped-flow UV-vis spectroscopy to investigate the formation of the peroxo-form of VCPO from the native-form after the addition of H₂O₂. The native-form had a characteristic peak at 315nm and upon formation of the peroxo-form of VCPO a peak appeared at 385nm. The pH dependence on the activity was also investigated experimentally within this study, revealing maximum stability at a pH value of 8.3, while maximum activity was observed at pH 5.0. These findings highlight the importance of understanding the protonation scheme within the active site.

The very center of the active site can be probed with ^{51}V NMR spectroscopy. Vanadium-containing peptides such as human transferrin,¹⁷ bovine apo-transferrin,¹⁸ and bovine prostatic acid phosphatase have been characterized by $\delta(^{51}\text{V})$ values between -515 to -542 ppm, and a number of model complexes are also within this area of the spectrum.¹⁹ The ^{51}V isotropic chemical shift for VBPO recorded by Rehder et al.¹⁸ in solution is -931 ppm for the native form, and -1135 ppm for the peroxy-form. Interestingly, the peroxy-resonance is shifted upfield by ca. -200 ppm from that of the native-form, in line with observations for small vanadates and peroxovanadates derived thereof. The experimental isotropic chemical shift of VPBO in the native-form is 400 ppm more shielded compared to typical vanadium complexes in solution, in particular VCPO, and also to the isotropic chemical shift extracted from the solid-state for VCPO.²⁰ Preliminary studies on the solid-state MAS spectrum of VBPO²¹ suggest an isotropic chemical shift of around -687 ppm, i.e. a smaller upfield shift (ca. -170 ppm) with respect to VCPO. An upfield shift was observed between QM/MM models of VCPO²² and VBPO,²³ although this upfield shift was smaller in magnitude than that observed experimentally.

Quantum-chemical computations can be an important structural tool for investigating the active sites of vanadium haloperoxidases. The structure of VCPO in the native-form was investigated using a number of different computational techniques, such as DFT,²⁴ TD-DFT,²⁵ QM/MM,^{22,26,27} and CPMD/MM simulations.²⁸ The first step in the catalytic cycle is believed to be protonation of the vanadate, and the QM/MM studies on the native-form of VCPO showed that a configuration containing an axial water and one hydroxo group in the equatorial plane is significantly lower in energy than any other configuration.²⁶ We have applied a QM/MM scheme to study various protonation states of the vanadate cofactor and its positional isomers for the native-form of VCPO.²² Based on a comparison between QM/MM-computed and experimental ^{51}V NMR chemical shift tensors, two doubly and one triply protonated forms emerged as most probable structural candidates for the resting state of the VCPO active site. Corresponding chemical-shift tensors have been predicted for the native form of VBPO.²³

Zampella et al.¹⁰ performed an active-site model study, using DFT, for both the native and peroxo-form of the VHPOs and considered the reaction energies combined with TD-DFT results when suggesting a singly protonated peroxovanadate as being the most likely candidate for the intermediate peroxo-form, as it had the best agreement with the UV-vis spectral band at 385nm. Identifying which of the two equatorial oxo ligands would be protonated within VHPO, either O¹ or O³, is a question that remains open at present.

The resolution of the solid-state structure of *p*-VCPO is not high enough to locate hydrogen atoms, and the uncertainty in the atom positions of heavier atoms makes it very speculative to differentiate between oxo and hydroxo bond lengths for the vanadate cofactor. Apparently, the crystallization of the VBPO enzyme is as yet unsuccessful for the peroxo-intermediate. In view of these current limitations in the experimental data we apply computational methods to probe and assess structural differences between these proteins, differences that may have important implications for their reactivities. Therefore the main aim of this present study is to investigate the protonation states of the intermediate peroxo-form of VHPOs, and critically compare the results to the previously investigated native-forms.

Computational methods

Protein Preparation

The same methods as in our previous studies on VCPO and VBPO were employed.^{22,23} The initial geometry of the *p*-VCPO enzyme was taken from the pdb file (1IDU.pdb), and the initial geometry of the *p*-VBPO enzyme was constructed from the pdb file of the *n*-VBPO (1QI9.pdb), obtained from the RCSB website.²⁹ As the experimental structure of *p*-VBPO is not available till date, we produced a ‘homology-type’ model. The VBPO file was modified by deleting the vanadium cofactor, and then the coordinates from the peroxy-form of the VCPO cofactor were transposed into the emptied active site of the native-form of VBPO (hereafter labeled *n*-VBPO). The *n*-VBPO is a homodimer. Our previous QM/MM studies²³ showed that two vanadium active sites are similar, and therefore only one such ‘homology-type’ model was studied, focusing only on one of the metal centers. The large degree of homology, particularly within the active site, provides validity to this approach. Protonation states of the titratable residues were assigned using the Propka program.³⁰ After selecting the protonation state of the active site (*vide supra*), neutrality was imposed on the models by selectively protonating residues on the surface of the protein which were $> 5 \text{ \AA}$ from the active centre (residues with higher *pKa* values were preferentially protonated). In order to provide a convenient comparison to the pure DFT work by Zampella et al.¹³ we consider a range of models, see Table 1.

The solvation of VCPO and VBPO was achieved by placing a 30 \AA solvent sphere of ‘TIP3 water’ (solvent model in CHARMM³¹) centered on a vanadate moiety. The solvation was performed iteratively with intermediate relaxation, and a boundary potential was imposed to prevent solvent ‘escaping’ during the model relaxation and equilibration phase. The vanadate moieties were also fixed at X-ray coordinates with an additional rigid constraint being applied to the vanadium histidine N^δ bonds during equilibration. The solvated proteins were relaxed via several cycles of molecular mechanics (MM) minimization and molecular dynamics (MD) simulations. Once each system was equilibrated (~200-400 picoseconds of MD simulation) six snapshots were taken at 30ps intervals along the MD trajectory for QM/MM optimizations, in order to generate a reasonable sample size with different protein configurations.³²

Table 1: Selected models labeled according to the protonation state (Z for zero, S for singly, and D for doubly protonated); the numbers refer to the oxygens that were protonated (1,2,3,4), see Figure 1 for the oxygen numbering convention.

Unprotonated	Singly protonated	Doubly protonated
<i>p</i> -VHPO-Z	<i>p</i> -VHPO-S1	<i>p</i> -VHPO-D13
	<i>p</i> -VHPO-S2	<i>p</i> -VHPO-D12 [†]
	<i>p</i> -VHPO-S3	<i>p</i> -VHPO-D14 [†]
	<i>p</i> -VHPO-S4	

[†] Only investigated for VCPO.

Results for QM regions I (small) and III (large) are herein presented for each of the selected models in Table 1, while those for an intermediate region II are deposited in the supporting information (SI). Figure 2 shows the segments of the residues and the crystallographic water molecules that are included in the QM I and III regions. Note that QM region III corresponds to QM region IV from our first study on native VCPO.²²

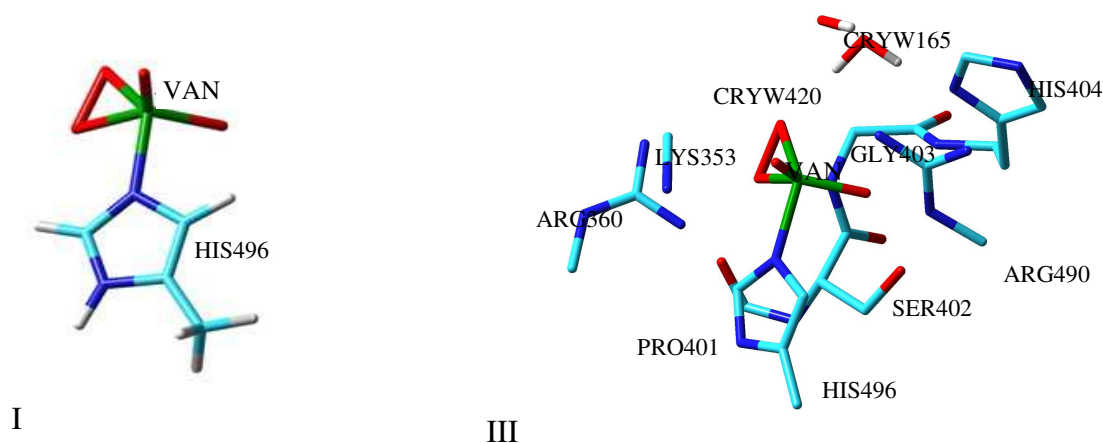


Figure 2. QM regions I and III for peroxo-form of haloperoxidases, deprotonated vanadate moiety shown as an example. The protons of the neighboring residues in QM region III were omitted from this figure for clarity.

ChemShell³³ was utilized as the QM/MM software suite. Turbomole³⁴ with the BP86³⁵ functional and the AE1 basis set was applied to the QM regions using the resolution of identity approximation, RI-BP86/AE1. The AE1 basis comprises the

Wachters basis³⁶ augmented with two diffuse *p* and one diffuse *d* sets for metal centers (8s7p4d, full contraction scheme 62111111/33111111/3111), and 6-31G*³⁷ for all other atoms in the QM region, together with suitable auxiliary fitting functions from the Turbomole library.³⁸ DL_POLY³⁹ provided the MM energy and gradients using the CHARMM27 force field.⁴⁰ An electrostatic embedding scheme was applied.⁴¹ Partial atomic charges for the vanadate moiety were created using Weinhold natural population analysis (NPA)⁴² from gas-phase models optimized at the RI-BP86/AE1 level of theory, see SI. The residues within 10 Å of the vanadium cofactor were included in the active MM region.

The magnetic shielding tensors and NQR tensors were computed using the Gaussian 03⁴³ package with the B3LYP⁴⁴ functional and the AE1+ basis (AE1 basis augmented with additional diffuse functions⁴⁵ on all non-hydrogen atoms). The protein and solvent surrounding the QM region were treated as fixed point charges. A single VOCl₃ molecule was used as a reference for the conversion to relative chemical shifts with a calculated isotropic magnetic shielding of -2294.4 ppm. The isotropic chemical shift δ_{iso} is defined as $\delta_{\text{iso}} = \sigma_{\text{iso}} - \sigma_{\text{VOCl}_3}$ where σ_{iso} is the isotropic shielding of the vanadium nucleus in the enzyme and σ_{VOCl_3} is the reference isotropic chemical shielding of VOCl₃. The Haeberlen–Mehring–Spiess⁴⁶ convention was used to define the principal components of the CSA and NQR tensors for consistency with our own previous work.^{22,23} The SIMPSON⁴⁷ software package was employed to simulate the spectra, using the parameters extracted from the above CSA and EFG tensors. TD-DFT computations were performed at the same B3LYP/AE1+ level, for a number of different models, at the QM/MM optimized geometries.

Results and discussion

Geometrical Details

Starting from the X-ray structures, a number of possible protonation states of the peroxovanadate cofactor were modeled using a previously described QM/MM optimization protocol.²² Because the constituent $V(O_2)O_2$ unit bears one overall negative charge and because neutral vanadates or peroxovanadates are usually not acting as strong Brønsted bases, an unprotonated (*p*-VHPO-Z) or a singly protonated state would seem as the most probable. Consistent with this expectation, most of the doubly protonated models that were considered turned out to be unstable with respect to maintaining the peroxo-coordinated geometry. For instance, QM/MM optimization of *p*-VCPO-D12 and *p*-VCPO-D14 resulted in partial detachment of the hydroperoxy ligand, which rearranged from the side-on η^2 coordination to an essentially end-on η^1 mode. Because of this clear disagreement with experiment, these models were not explored further. The only stable doubly protonated species was *p*-VHPO-D13. Salient distances of all final *p*-VCPO models are summarized in Table 2, those of the corresponding *p*-VBPO homologues are deposited in Table S1b of the supporting information (SI).

The bond lengths of the peroxovanadate cofactor fall within the expected range, ca. 1.6-1.7 Å for vanadium oxo bonds (V=O), 1.8-1.9 Å for vanadium hydroxo (V-OH) and peroxo bonds (V-(O₂)), and 2.0- 2.1 Å for the V-N bond to HIS496.. As the standard deviations across the six snapshots for the bond lengths of the peroxovanadate cofactor are rather small, all the models are generally very similar within the six selected snapshots. The geometric convergence for the individual models is comparable to our prior QM/MM optimizations of the native VHPO forms,²² indicating that the active site is rather rigid, and that the use of a small number of snapshots seems valid. Furthermore, a good degree of similarity is observed between the bond lengths of the peroxovanadate, across many of the different protonated models of *p*-VCPO and *p*-VBPO, see Tables 2 and S1b, respectively.

Table 2: Bond lengths involving vanadium cofactor for QM/MM regions I and III of *p*-VCPO.^a

		V-N ^{HIS 496}	V-O ¹	V-O ²	V-O ³	V-O ⁴	O ² -O ⁴	V-O ^{wat} ^b	MAD(Δ_{MAX}) ^c	MAD(Δ_{MAX}) ^c
X-ray <i>p</i> -VCPO		2.19	1.93	1.89	1.60	1.86	1.47	4.39	(including V-O ^{wat})	(without V-O ^{wat})
<i>p</i> -VCPO-Z	I	2.06(0.01)	1.68(0.00)	1.89(0.00)	1.65(0.00)	1.87(0.01)	1.47(0.00)	4.02(0.57) ^d	0.12(0.37) ^h	0.07(0.25) ^f
	III	2.06(0.01)	1.67(0.00)	1.93(0.01)	1.66(0.00)	1.87(0.00)	1.47(0.00)	3.90(0.22)	0.14(0.49) ^h	0.08(0.26) ^f
<i>p</i> -VCPO-S1	I	2.03(0.01)	1.83(0.00)	1.87(0.00)	1.61(0.00)	1.84(0.00)	1.45(0.00)	2.64(0.01) ^d	0.30(1.75) ^h	0.06(0.16) ^e
	III	2.13(0.00)	1.88(0.00)	1.88(0.00)	1.62(0.00)	1.86(0.00)	1.45(0.00)	2.13(0.01)	0.35(2.26) ^h	0.03(0.06) ^e
<i>p</i> -VCPO-S2	I	2.06(0.02)	1.65(0.01)	2.10(0.03)	1.63(0.00)	1.90(0.01)	1.47(0.01)	3.11(0.60) ^d	0.21(1.28) ^h	0.12(0.28) ^f
	III	2.13(0.04)	1.66(0.00)	2.11(0.06)	1.65(0.01)	1.89(0.02)	1.47(0.01)	2.51(0.31)	0.36(1.88) ^h	0.11(0.27) ^f
<i>p</i> -VCPO-S3	I	2.04(0.02)	1.63(0.00)	1.85(0.00)	1.81(0.02)	1.85(0.01)	1.45(0.00)	2.89(0.73) ^d	0.32(1.50) ^h	0.12(0.21) ^g
	III	2.13(0.04)	1.64(0.00)	1.87(0.01)	1.86(0.02)	1.87(0.01)	1.45(0.00)	2.15(0.10)	0.41(2.24) ^h	0.11(0.26) ^g
<i>p</i> -VCPO-S4	I	2.04(0.01)	1.64(0.00)	1.94(0.00)	1.63(0.01)	2.05(0.00)	1.47(0.00)	3.15(0.36) ^d	0.28(1.24) ^h	0.12(0.29) ^f
	III	2.06(0.01)	1.66(0.00)	1.94(0.00)	1.66(0.00)	1.88(0.00) ^h	1.47(0.00)	3.68(0.01)	0.18(0.71) ^h	0.09(0.27) ^f
<i>p</i> -VCPO-D13	I	2.05(0.01)	1.78(0.00)	1.82(0.02)	1.77(0.00)	1.84(0.02)	1.42(0.01)	2.30(0.01) ^d	0.38(2.09) ^h	0.10(0.17) ^g
	III	2.08(0.01)	1.83(0.00)	1.82(0.00)	1.77(0.01)	1.83(0.00)	1.43(0.00)	2.11(0.01)	0.40(2.28) ^h	0.09(0.17) ^g

^a Mean bond lengths and standard deviations are reported in Å, X-ray refined experimental values of *p*-VCPO are shown for comparison. ^b O^{wat} is in the MM region for the small QM I models. ^c MAD is the mean absolute deviation ($|\overline{\Delta}|$, where $\Delta = r_{\text{vcpo}} - r_{\text{exp}}$) and Δ_{MAX} is the maximum deviation relative to the X-ray distances of 1IDU.pdb (with and without V-O^{wat}, see text). ^d Water in MM region. ^e Δ_{MAX} observed for V-N^{HIS}. ^f Δ_{MAX} observed for V-O¹. ^g Δ_{MAX} observed for V-O³. ^h Proton transfers to HIS404. ^h Δ_{MAX} observed for V-O^{wat}.

The X-ray structure of *p*-VCPO with a resolution of 2.24 Å determined by Messerschmidt et al.⁸ shows the terminal oxo ligands O³ and O¹ at distances of 1.60 Å and 1.93 Å, respectively, suggesting that these atoms are unprotonated (V=O) and protonated (V-OH), respectively. The QM/MM-optimized bond distances from vanadium to the O³ and O¹ ligands for the *p*-VCPO-S1 model fit best to the experimentally refined values, however the experimental uncertainty is too large to provide definitive conclusions. All other models that are not protonated at O¹ have the V-O¹ bond length elongated by up to 0.27 Å relative to the X-ray structure.

The rather long refined V-O¹ distance might also nurture the speculation that this O atom could be doubly protonated, i.e. be present as a water ligand. In fact, the resulting ligand environment about the metal would be reminiscent of VO(O₂)(H₂O)_n⁺, the formulation of peroxovanadate at low pH. Because the nearby Arg360 residue is probably protonated and a good H-bond donor, this situation is unlikely so that we did not set up and prepare any *p*-VHPO-D11 models from the onset. In order to test this expectation, we constructed such a model from one of the *p*-VCPO-S1 minima (optimized with QM region III) by manually moving the proton from Arg360 to O¹. During optimization of this *p*-VHPO-D11 structure with a neutral Arg, the proton jumped back to the arginine, affording the regular *p*-VCPO-S1 model.

In general, most of the vanadium-ligand bond distances increase between ~0.01 to ~0.05 Å when going from the smaller QM region I to the larger QM III region. In contrast, the V-O⁴ bond in the singly protonated model *p*-VCPO-S4 shortens by about 0.17 Å when going from the smaller to the larger QM III region. This is attributed to a proton transfer from the O⁴ ligand to a crystal water, and a subsequent proton transfer to the neighboring HIS404, which occurred spontaneously during optimization. This creates an active site which is structurally similar to the originally unprotonated model, *p*-VCPO-Z, except for an additionally charged histidine group (HIS404). This occurs for both the *p*-VCPO and *p*-VBPO active sites, see Tables 1 and S2b, respectively. Likewise, for *p*-VBPO-S3 the proton is transferred from the O³ ligand to HIS404 during QM/MM optimisation with QM region II, but the same proton hops back to O³ during optimization with QM region III (no such event occurred with the corresponding *p*-VCPO models).

The distance between the vanadium and N^{HIS496} is typically shorter in the QM/MM optimized models than in the X-ray structure, by up to 0.13Å for *p*-VCPO-Z and *p*-VCPO-S4; smaller deviations are typically seen when a crystal water molecule becomes bound to the peroxovanadate center, as in the other singly protonated models. The computed V-N^{HIS496} distances vary between 2.06Å up to 2.19Å for the *p*-VCPO models, while they range from 2.3Å to 2.6Å in the native VCPO forms, suggesting that peroxovanadate binds more strongly than vanadate to HIS496. This trend has already been observed by Renirie et al.,⁹ and aqueous peroxovanadate has been found to bind imidazole more strongly than vanadate.⁴⁸

Typically the QM/MM-optimized bond distances of *p*-VCPO and *p*-VBPO, with the same protonation state of the peroxovanadate cofactor, show little variation between these two proteins, which adds support to the validity of homology modeling in the case of *p*-VBPO.

The *p*-VCPO-Z and the related *p*-VCPO-S4 models (essentially *p*-VCPO-Z with protonated HIS) contain an empty cavity above the peroxovanadate moiety, in agreement with the X-ray structure. The remaining models contain a water molecule in this position, with a computed distance short enough to be considered bound to the metal (V-O distances between 2.1 and 2.5 Å), in apparent disagreement with experiment, where this site remains empty.

It is difficult at this point to judge the significance of the seemingly empty coordination site in the solid-state structure. If this site is truly vacant, *p*-VCPO-Z and *p*-VCPO-S4 would fit much better to the refined coordinates than all other models. For these two models, the mean absolute deviation (MAD) between all optimized and experimental bond lengths in Table 2 amounts to 0.14 and 0.18 Å, respectively (QM region III), whereas those of the other candidates approach or exceed 0.4 Å (see last but one column in Table 2). If, on the other hand, this site was occupied by a very mobile or labile water ligand, the latter might well escape detection in the X-ray analysis, given the low resolution presently achievable. In that case, i.e. when the V-O^{wat} distance is disregarded in the analysis, the resulting MAD is lowest for the *p*-VCPO-S1 model (0.03Å, see last column in Table 2) and shows little variation across the remaining models, typically around 0.1Å. We refrain from making structural

assignments based on these data and note that essentially all models presented in Table 2 could be viable candidates, with a slight preference for *p*-VCPO-Z and *p*-VCPO-S1 (or, perhaps, an equilibrium mixture between both).

In this context the intrinsic water binding energy of the pristine $V(O_2)O(OH)(H_2O)(Im)$ fragment (Im = methyl-imidazole) common to all *p*-VCPO-S models is of interest. Starting from the corresponding coordinates of the *p*-VCPO-S1 minimum obtained with QM region II, this complex was optimized in the gas phase. In the resulting minimum, the $V-O^{wat}$ distance is 2.35 Å. At the RI-BP86/AE1 level, water dissociation affording $V(O_2)O(OH)(Im)$ is computed to be endothermic by 11.5 kcal/mol (6.0 kcal/mol when corrected for basis-set superposition error). The water is thus indicated to be weakly bound. An attempt to optimize a non-protonated hydrated complex, i.e. $[V(O_2)O_2(H_2O)(Im)]^-$, resulted in detachment of the water ligand from the metal, in agreement with the results from the full QM/MM computations.

Hydrogen bonding

In all of the above-considered models of *p*-VCPO the HIS404 residue (which is included in QM region III) is no longer hydrogen bonded to the peroxovanadate cofactor, see Figure 1. This residue acts as a hydrogen bond acceptor from the nearest solvent water molecule, which in turn donates a hydrogen bond to the peroxovanadate cofactor. The O^1 ligand of the peroxovanadate is hydrogen bonded to ARG360 and ARG490. The singly protonated *p*-VCPO-S1 model no longer forms a hydrogen bond with ARG490, as compared to its native counterpart, and this is also observed for the *p*-VCPO-D13 doubly protonated models. This causes a gross structural deviation relative to the other models, as seen in overlay of all the models in Figure S2 of the SI, and the RMSD is much larger for *p*-VCPO-D13 when compared to other protonated and unprotonated models.

The LYS353 residue in *p*-VCPO, like the corresponding LYS341 in *p*-VBPO, forms a strong hydrogen bond to the O^2 peroxo oxygen ligand. This hydrogen bond is generally believed to induce the bond polarization necessary for the heterolytic cleavage of the side-on-bound peroxide.¹⁰ The major difference in the active sites of *p*-VCPO and the homology-modeled *p*-VBPO is a HIS411 in the position

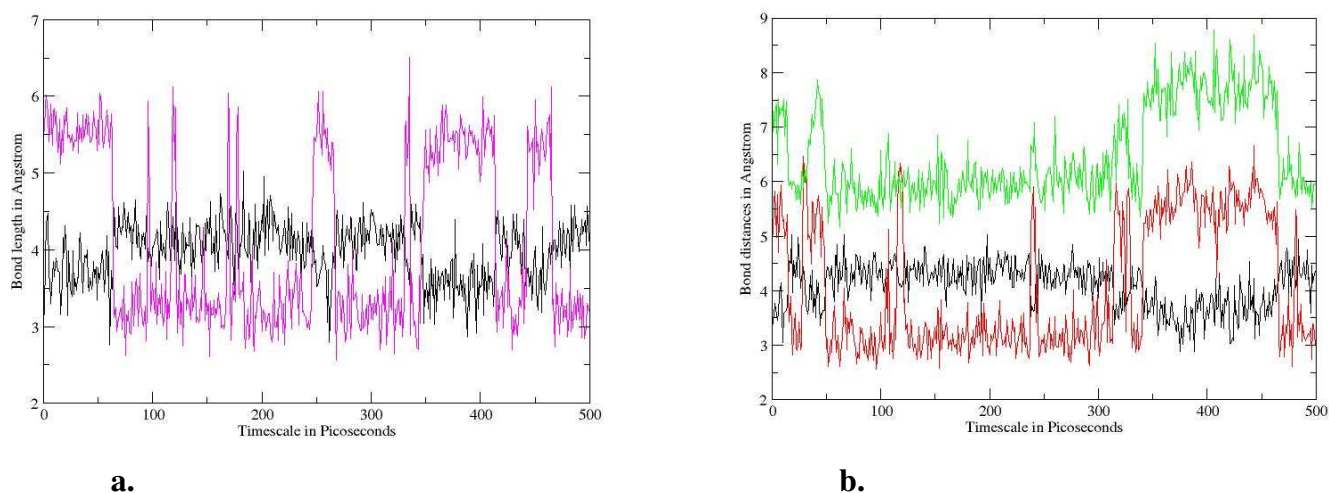
corresponding to a PHE397 in the *p*-VCPO. Since the HIS411 is within hydrogen bonding distance of LYS353, it has been suggested⁴⁹ that this residue in VBPO may form significant hydrogen bonds, thereby indirectly altering the reactivity of the enzyme. Previous site-directed mutagenesis studies have confirmed that these residues are crucial for activity.^{16,50} This HIS411 may affect the reactivity, by either protonating or deprotonating the LYS353, thereby indirectly affecting the oxidative strength of these enzymes and their affinity for the halide. To understand the possible roles of the HIS411, a set of calculations were performed with HIS411 in a flipped conformation, that is, rotating the aromatic group of HIS residue so that the N^ε atom is facing away from the LYS341. The resolution of the X-ray structure makes it difficult to distinguish clearly between N and C atoms in the five-membered rings of histidine residues, and hence, special attention is called to the two possible orientations. Such a rotated HIS411 residue is stable only for two models, *p*-VBPO-Z and *p*-VBPO-S1, see SI, and for the rest of the models it flipped back to the original position during the QM/MM optimization. In this original position, HIS411 is not involved in any direct H-bonding interactions with the peroxovanadate moiety. Likewise, the flipped *p*-VBPO-S1 model is devoid of such direct interactions. This finding is consistent with the typically rather small differences between computed structural and NMR parameters of the same VCPO and VBPO models (see below). Only for flipped *p*-VBPO-Z a persistent hydrogen bond between HIS411 and O⁴ of the peroxo unit was encountered. Even in this case, however, the resulting ⁵¹V NMR tensor elements were found to be hardly affected by this interaction (see discussion below and data in the SI).

To summarize this part, the non- and singly protonated models *p*-VCPO-Z and *p*-VCPO-S1 appear to be the best candidates for the protonation state of *p*-VCPO. It is difficult to exclude all the other models, however, and many of these may be further regarded as possible candidates. A comparable degree of similarity was also observed in our earlier studies on the native-forms of VCPO and VBPO. The lack of *p*-VBPO X-ray data prevents a similar type of analysis for this enzyme at present.

Solvation

As the apical oxygen (O⁴) in the native-form of VCPO is released and the peroxide binds side-on (O₂ in the equatorial plane and O₄ in a pseudo-axial position) to the

vanadium, an empty coordination site is generated and is able to accept the chloride ion during the catalytic cycle. In the crystallographic structure of *p*-VCPO, the nearest water molecules are about 4.4 Å and 5.7 Å away from the metal center, leaving a visibly large empty space at the latter. During the MD equilibration of *p*-VCPO-Z, these two water molecules diffuse closer to the vanadium, occupying this void that exists in the experimentally determined structure. The solvent molecules, Cryw420 and Cryw165, oscillate between ~3 and ~5.5 Å from the vanadium, due to an interchange of their positions, which is shown in Figure 4a. Whether this void can accommodate any additional water molecules that are as yet unidentified crystallographically, is an important question that may have mechanistic consequences.⁵¹



a. **b.**
Figure 4: Plot of the distances between vanadium and the oxygen atoms of the nearest solvent molecules during MD initial equilibration. **a.** The crystal water molecule Cryw420 (black) and Cryw165 (pink) **b.** The crystal water molecule Cryw420 (black) and the additional water molecules SOLV_z(red) and SOLV_y(green), that were manually added during the solvation phase.

To probe if such an unidentified water molecule could have been missed by our standard solvation/equilibration protocol, three additional water molecules were placed manually into this cavity of *p*-VCPO-Z and a series of classical molecular dynamics simulations were performed. The additional solvent molecules were found to interchange with one of the two crystal water molecules within the active site, subsequently undergoing the same oscillation of ~3 or ~5.5 Å from the vanadium

throughout the MD simulation, see Figure 4b. Such frequent exchange processes are an indication of low barriers, presumably due to weak interactions. In general, there appears to be only sufficient room for two water molecules close to the metal, either one of the two crystallographically observed, or one of the added waters. The overall effect of the additional water is only marginal on the isotopic chemical shifts, typically less than 10ppm, as discussed in further detail below.

Isotropic chemical shifts

We have investigated whether ^{51}V chemical shifts may act as a useful probe for the assignment of protonation states of the peroxovanadate active site in vanadium haloperoxidase enzymes. The ^{51}V chemical shifts (δ_{iso}) of the vanadium nuclei in the different QM regions are given in Table 3 (computed with inclusion of the MM point charges).

Table 3: ^{51}V Isotropic chemical shifts (ppm) averaged over six snapshots for the two regions, together with the corresponding standard deviations. $\overline{\Delta}_\delta$ and $\overline{|\Delta|}_\delta$ are the mean signed and mean absolute deviations between the VCPO and VBPO models.

Model ID	QM region I		QM region III	
	<i>p</i> -VCPO	<i>p</i> -VBPO	<i>p</i> -VCPO	<i>p</i> -VBPO
Z	-704 ± 7	-708 ± 6	-696 ± 8	-693 ± 15
S1	-611 ± 3	-668 ± 13	-683 ± 20	-757 ± 21
S2	-741 ± 13	-694 ± 64	-700 ± 30	-735 ± 30
S3	-599 ± 23	-612 ± 17	-658 ± 35	-617 ± 34
S4	-751 ± 7	-755 ± 9	-739 ± 6	-703 ± 16
D13	-227 ± 10	-327 ± 5	-379 ± 28	-428 ± 9
$\overline{\Delta}_\delta$ ($\overline{ \Delta }_\delta$)	58(58)		-9 (41)	

The isotropic chemical shifts across the QM regions I-III are fairly stable, where variations typically amount to less than 30ppm for most of the models (*p*-VHPO-Z, *p*-VCPO-S2,S4 and *p*-VBPO-S2,S3). The other models show larger fluctuations, with more significant shielding occurring on going from QM region I to III, up to ca. -90ppm. This shielding may be partially attributed to the binding of the apical water molecule as it gets included in the larger QM region (see discussion above). In the following, we will focus on the QM III results. For the isotropic chemical shifts there

are some notable differences between *p*-VCPO and *p*-VBPO models, cf. the $\overline{|\Delta|}_\delta$ value of ca. 40 ppm in Table 3. The isotropic chemical shifts may be loosely collected together into two groups, based on their locations. Firstly, a downfield region from around ca. -400ppm has the doubly protonated models located within it. Secondly, an upfield region from -620 to -760ppm contains all singly and non-protonated models, with the S4 and S1 models representing the more upfield of these shifts for the *p*-VCPO and *p*-VBPO proteins, respectively.

Comparison of these isotropic shifts with experiment is hampered by the fact that only a single value is known, namely that of *p*-VBPO in solution at $\delta = -1135$ ppm.¹⁸ None of the computed values comes even close to this exceptionally shielded region. The same had been noted for the native VBPO, where the solution $\delta(^{51}\text{V})$ value of -931 ppm reported in the same study was reproduced neither computationally²³ nor in a preliminary solid-state NMR study of the same enzyme.²¹ What is clear, however, is that transformation of the native into the peroxo form entails a substantial shielding of the ^{51}V resonance, by ca. -200 ppm according to the VBPO solution study.

Assessment of the corresponding trend for the QM/MM data depends noticeably on the particular model(s) used for the native forms. For instance, the three VCPO models that have reproduced the solid-state ^{51}V NMR-tensor elements reasonably well, VCPO-D14, -D34, and -T144, showed isotropic $\delta(^{51}\text{V})$ values of -580, -607, and -602 ppm, respectively (largest QM region).²² Except for the diprotonated *p*-VCPO-D13, all other *p*-VCPO models show clear upfield shifts from these numbers. For the *p*-VCPO-Z and *p*-VCPO-S1 variants, which emerged as particularly promising from the structural parameters discussed above, this computed upfield shift is between ca. -80 ppm and -120 ppm. Comparing the same VBPO and *p*-VBPO models with each other⁵² affords computed upfield shifts around ca. -70 to -160 ppm. These (and the other singly protonated) models thus reproduce the observed trend qualitatively reasonably well. The quantitative underestimation of this effect may be rooted in shortcomings of the particular exchange-correlation functionals employed as these have shown problems to accurately reproduce similar trends between simple aqueous vanadate and peroxovanadate complexes.⁵³ In any event the qualitative agreement with experimental trend for most of the QM/MM models is encouraging. One model for each enzyme fails to reproduce this trend, namely the doubly protonated *p*-VHPO-

D13, for which substantial downfield shifts are computed (Table 3). This candidate can thus be safely excluded.

Table 4: Reduced anisotropy δ_σ (ppm), asymmetry η_σ , nuclear quadrupole coupling constant C_Q (MHz) and asymmetry parameter η_Q with the associated standard deviations for six individual snapshots of a given model. MAPD is the mean absolute percent deviation across the four parameters relative to the average values for the S1 model (QM region III) of the respective haloperoxidases.

Model	<i>p</i> -VCPO	δ_σ	η_σ	C_Q	η_Q	MAPD
ID	<i>p</i> -VBPO ^a					
Z	I	-685 ± 9	0.4 ± 0.01	9 ± 0.35	0.30 ± 0.14	
	I	-729 ± 7	0.3 ± 0.01	8 ± 0.12	0.25 ± 0.05	
	III	-699 ± 6	0.3 ± 0.03	8 ± 0.36	0.28 ± 0.22	44
	III	-695 ± 11	0.3 ± 0.06	8 ± 0.24	0.18 ± 0.06	52
S1	I	-809 ± 4	0.6 ± 0.01	-8 ± 0.06	0.84 ± 0.03	
	I	-750 ± 12	0.6 ± 0.04	-8 ± 0.02	0.34 ± 0.04	
	III	-923 ± 6	0.8 ± 0.04	6 ± 0.30	0.65 ± 0.06	--
	III	-1014 ± 5	0.5 ± 0.03	5 ± 0.45	0.86 ± 0.10	--
S2	I	-668 ± 40	0.23 ± 0.03	9 ± 0.26	0.82 ± 0.10	
	I	-501 ± 108	0.60 ± 0.26	9 ± 1.29	0.93 ± 0.02	
	III	-739 ± 93	0.19 ± 0.08	12 ± 2.34	0.44 ± 0.13	57
	III	-618 ± 59	0.20 ± 0.10	8 ± 0.20	0.80 ± 0.13	42
S3	I	-800 ± 38	0.7 ± 0.02	4 ± 0.11	0.47 ± 0.35	
	I	-708 ± 29	0.7 ± 0.03	7 ± 0.59	0.74 ± 0.17	
	III	-901 ± 35	0.8 ± 0.18	7 ± 1.57	0.52 ± 0.34	10
	III	-716 ± 74	0.7 ± 0.19	8 ± 1.63	0.67 ± 0.19	37
S4	I	-800 ± 23	0.9 ± 0.01	13 ± 0.42	0.64 ± 0.05	
	I	-772 ± 8	0.1 ± 0.02	13 ± 0.41	0.32 ± 0.03	
	III	-672 ± 6	0.21 ± 0.00	7 ± 0.04	0.18 ± 0.03	47
	III	-674 ± 17	0.3 ± 0.06	7 ± 0.58	0.24 ± 0.08	46
D13	I	1070 ± 10	0.7 ± 0.03	10 ± 0.57	0.62 ± 0.11	
	I	981 ± 19	0.9 ± 0.04	9 ± 0.29	0.45 ± 0.06	
	III	1107 ± 34	0.7 ± 0.02	5 ± 0.24	0.79 ± 0.27	68
	III	-1028 ± 18	0.9 ± 0.04	10 ± 0.93	0.04 ± 0.02	69

^aBoldface entries refer to *p*-VBPO.

Anisotropic chemical shifts

The four parameters that characterize an experimental ^{51}V spectrum are the reduced anisotropy δ_σ , the asymmetry parameter η_σ , the nuclear quadrupole coupling constant C_Q (MHz), and the asymmetry parameter of the EFG tensor η_Q . These parameters are computed from the CSA and EFG tensors obtained from the QM/MM-optimized models of *p*-VCPO and *p*-VBPO, and are collected in Table 4.

In general, small variations are observed in the calculated CSA and EFG values across the six snapshots. There are variations in the reduced anisotropy (δ_σ) when increasing the size of the QM region for all models, and these variations are heavily dependent upon the distance of the crystal water to the vanadium metal center, for example *p*-VCPO-S1 and *p*-VBPO-S1 models. They are also particularly pronounced for both the *p*-VCPO-S4 and *p*-VBPO-S4 models, which can be traced back to the proton transfer concomitant with the increase of the QM region. For the *p*-VBPO-S3 model, where a similar intermittent proton transfer was observed (see section on Geometric Details above), the variation in the reduced anisotropy is less pronounced.

Considering the MAPD in Table 4, which are given relative to the *p*-VHPO-S1 models, it is apparent that there are substantial differences between the various candidates. The *p*-VHPO-S1 models are simply chosen as a reference since they are strong candidates. These differences can be even better appreciated in the spectra that are simulated using the QM/MM data (Figure 5). These results thus provide a promising avenue of discriminating between the likely candidates, once the corresponding experimental data becomes available.

In particular, the breadth of the experimental spectrum should be a good indicator for the protonation state, i.e. non- vs. singly protonated (compare, e.g. Figure 5a with 5c/e). It remains unclear at present whether the differences within the singly protonated models will be sufficient for specific assignments of the protonation site. According to the calculations, the differences should be more prominent for *p*-VPBO, which therefore appears to a better experimental target than *p*-VCPO for solid-state MAS ^{51}V NMR spectroscopy.

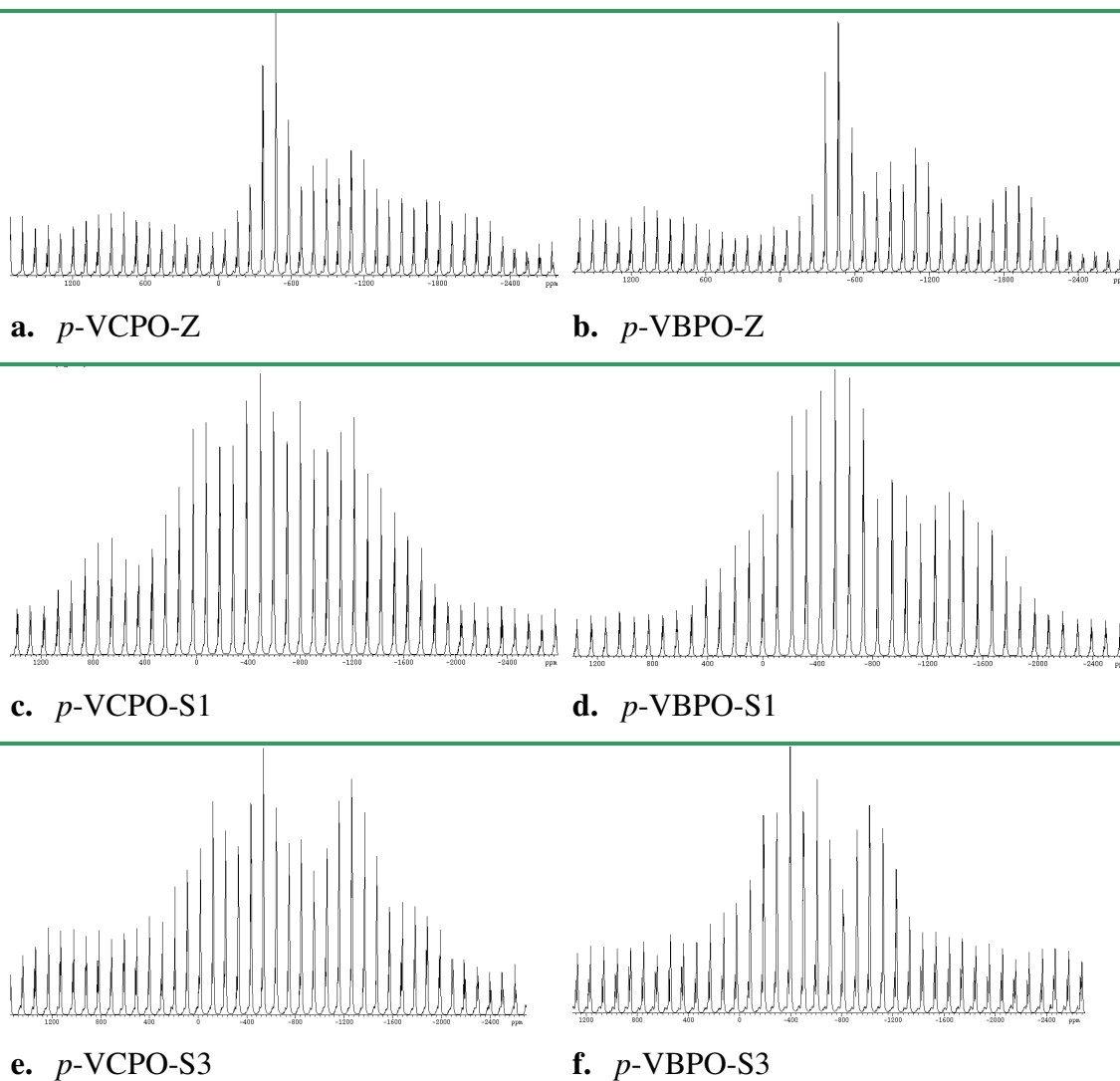


Figure 5: Simulated spectra of **a.** *p*-VCPO-Z, **b.** *p*-VBPO-Z, **c.** *p*-VCPO-S1, **d.** *p*-VBPO-S1 **e.** *p*-VCPO-S3, **f.** *p*-VBPO-S3, to visualize the difference between the unprotonated and singly protonated candidates in both *p*-VCPO and *p*-VBPO.

When the same *p*-VCPO and *p*-VBPO models are compared with each other, the variations in the tensorial properties are much less pronounced than when going from one protonation model to another. To appreciate the difference between a VHPO protein in the native or in the peroxy-form, illustrative examples of simulated ^{51}V NMR spectra for VCPO are given in Figure 6a and 6b.

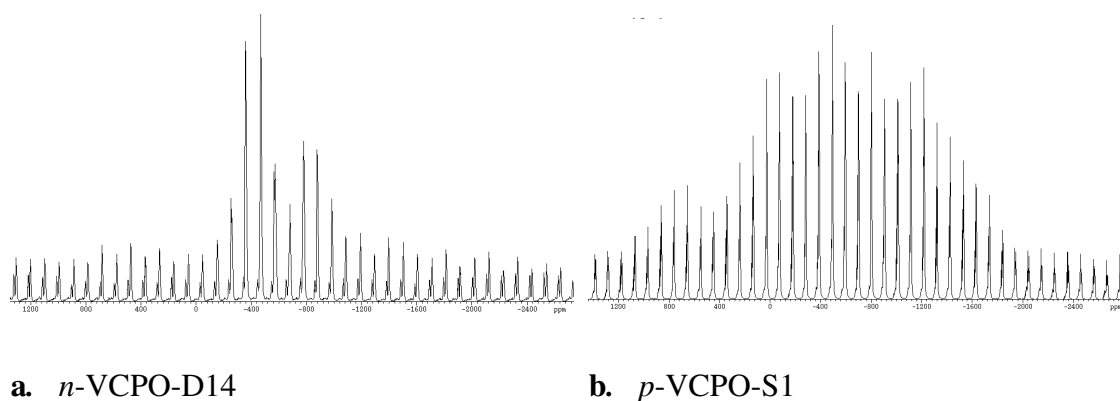


Figure 6: Simulated spectra for one of the best candidates of the native-form of VCPO, **a.** VCPO-D14, compared to one of the best candidates for the peroxo-form, **b.** *p*-VCPO-S1.

As in our previous studies on the native enzymes, we assessed the direct effect of the surrounding peptide regions on the ^{51}V NMR and EFG tensors by simply deleting the point charges from the MM part in the property computation. The corresponding results, deposited in the SI and denoted by an asterisk, show similar trends as the tensor values for the full models given in Table 3. We also checked for selected models that the inclusion of additional water molecules in the apical cavity discussed above (data denoted by a double asterisk in the SI), or the possible ring-flip of the extra HIS411 in *p*-VBPO (denoted by a dagger in the SI), have only minor effects on the computed NMR and EFG tensors of the metal center.

TD-DFT

TD-DFT was employed to calculate electronic excitation energies from the QM/MM optimized models of both the native and peroxo-forms of VCPO and VBPO. Despite the known deficiencies of TD-DFT for long-range charge-transfer states,⁵⁴ this method has proven to be very promising for many transition-metal systems⁵⁵ and has recently been used to assess the protonation state of native VCPO.²⁷ Results for the two strongest, low-lying excitations for the *p*-VCPO and *p*-VBPO models are presented in Table 5. The last column of Table 5 shows the difference between the calculated excitation energy for the most intense of these two bands (QM I region) and the experimentally observed absorption band at 384nm reported by Renirie et al.⁹ We list only results for the smaller QM region I because those for the larger QM

region III were plagued by spurious long-range charge transfer states (e.g. from a lone pair on a distant peptide N atom to an empty metal-centered MO). In a series of test calculations on the *p*-VCPO-Z model, only small differences between the snapshots were observed, and therefore only results for a single snapshot are presented in Table 5.

Table 5: The transition energy λ in nm, the oscillator strength (f), and the coefficients (C_{ij}) of the CI expansion from TD-DFT calculations of the peroxo-form of *p*-VCPO and *p*-VBPO (QM region I). Δ denotes the difference between the calculated absorption maximum and the experimental absorption maximum at 384nm.

Model ^a	$\lambda_{nm}(f)$	Dominant Contribution		C_{ij}	$\Delta(\lambda - 384)$
<i>p</i> -VCPO-Z	336(0.01)	H	→ L	0.532	-48
	292(0.01)	H-1	→ L	0.608	
<i>p</i>-VBPO-Z	335(0.009)	H	→ L+1	0.457	-49
	297(0.007)	H	→ L	0.615	
<i>p</i> -VCPO-S1	320(0.03)	H-2	→ L	0.567	-8
	376(0.03)	H	→ L+1	0.693	
<i>p</i>-VBPO-S1	469(0.006)	H	→ L	0.490	43
	427(0.006)	H	→ L	0.495	
<i>p</i> -VCPO-S2	331(0.01)	H	→ L+2	0.661	-53
	336(0.01)	H-1	→ L+1	0.461	
<i>P</i>-VBPO-S2	329(0.008)	H	→ L+1	0.697	-55
	292(0.004)	H-2	→ L	0.573	
<i>p</i> -VCPO-S3	453(0.01)	H	→ L	0.669	69
	407(0.01)	H-1	→ L	0.601	
<i>p</i>-VBPO-S3	457(0.006)	H	→ L	0.653	73
	342(0.005)	H-1	→ L+1	0.587	
<i>p</i> -VCPO-D13	773(0.01)	H	→ L	0.687	389
	396(0.01)	H-1	→ L	0.671	
<i>p</i>-VBPO-D13	739(0.01)	H	→ L	0.678	355
	437(0.06)	H-1	→ L+1	0.582	

^aNo results are given for *p*-VHPO-S4 models, because they are not stable as such when the size of the QM region is increased.

In most cases there are two close-lying absorptions with similar intensities, which would probably not be resolved, as the UV-vis absorption bands reported for *p*-

VCPO⁵⁶ or *p*-VBPO⁵⁷ are very broad. According to visual inspection of the MOs involved (QM I region) the excitations occur predominantly from the occupied π -orbitals on the imidazole ring of HIS496/486, or an occupied π^* orbital on the peroxy moiety, into anti-bonding orbitals with a large d-character on vanadium.

Most models agree with experiment within ca. 50 nm (or ca. 0.4 eV - 0.5 eV in excitation energies), a rather modest accuracy for TD-DFT, and it is difficult to assign or exclude one particular model based on these data. The TD-DFT calculations of the VCPO-D13 and VBPO-D13 models have transition energies in the red region of the visible spectrum and are therefore considered less likely candidates.

In the resting native-form of the VCPO enzyme, the UV-vis band appears at 305 nm - 315nm, depending on the pH value.⁹ TD-DFT computations for selected native VCPO and VBPO models furnished strong absorptions in the observed region, again without clear distinctions for specific protonation states (see SI). The computed changes between the native and peroxy forms are more significant than differences between the two proteins at a particular stage of the catalytic cycle, as seen above for anisotropic chemical shifts. Interestingly the difference between VCPO and VBPO appears more pronounced in the peroxy-form. For the parent vanadate, H_2VO_4^- , a band at ca. 260 nm is computed,⁵⁸ i.e. distinctly blue-shifted relative to the vanadate cofactors in the enzymes and in good accord with experiment ($\lambda = 270$ nm).⁵⁶

Conclusions

We have used a QM/MM scheme to compute structures, ⁵¹V NMR tensors, and UV-Vis excitation energies of two vanadium-dependent haloperoxidases in their peroxy forms, namely *p*-VCPO and *p*-VBPO. The latter has been modeled for the first time, assuming homology of the active site with that of *p*-VCPO, for which the structure is known in the solid. Special attention was called to the dependence of the properties on the protonation state of the peroxovanadate moiety and the ensuing hydrogen-bond network. The ligand environment about the metal as observed in solid *p*-VCPO is best

preserved in the unprotonated models, whereas most of the singly protonated variants bind a nearby water molecule, which is present as free crystal water in the solid. Judging from the agreement of optimized bond lengths and the isotropic ^{51}V chemical shifts with experiment, the non- or singly protonated models are the most likely structural candidates for these enzymes. Models that are doubly protonated (whether at the terminal oxo or the peroxy atoms) can be excluded, as they are either unstable during optimization, or afford isotropic chemical shifts that fail to reproduce the experimentally observed increase in shielding on going from native to peroxy forms.

For a further discrimination between non- and singly protonated models (and the specific site of protonation in the latter), isotropic chemical shifts and TDDFT-derived excitation energies are not sufficient. Theoretical chemical-shift and EFG tensors, on the other hand, predict substantial intrinsic differences between the various protonation models, in particular between non- and singly protonated ones. When an experimental solid-state ^{51}V MAS NMR of *p*-VCPO or *p*-VBPO will be reported eventually, a comparison to the simulated spectra reported herein should enable the discrimination between the possible candidates and furnish detailed insights into the structure of the active site.

The VCPO and VBPO proteins have been experimentally shown to have a different oxidation profile. Whether this is a result of a single step in the catalytic cycle or whether this is a fundamental difference throughout the cycle is a question that may be addressed systematically with QM/MM calculations. This study takes the first steps toward answering this question, as it was shown that the secondary environment of the proteins, i.e. outside the first hydrogen bonding sphere, effectively tunes the properties of the active site via indirect hydrogen bonds and electrostatic interactions. The subtle differences between the active sites of both native and peroxy forms of VCPO and VBPO are best probed by the anisotropic ^{51}V NMR properties, i.e. CSA and EFG tensors.

In summary, we have successfully analyzed a challenging reactive intermediate by using a combination of theoretical methods for a comprehensive comparison to a number of previously published experimental reports. The multidisciplinary nature of this comparison serves to gauge the strengths of the various theoretical approaches

and to increase the confidence in the results. New interpretations of available experimental data, and predictions where such data is currently lacking, open the way for further studies on these intriguing systems.

Acknowledgements

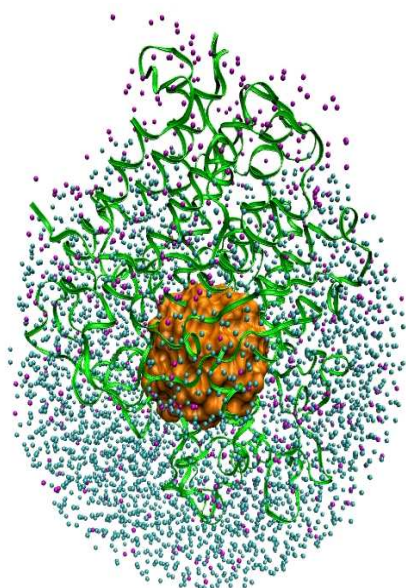
M.B. wishes to acknowledge the Deutsche Forschungsgemeinschaft for support. Computations were performed on a local computer cluster of Intel Xeon and Opteron PCs at the MPI Mülheim, maintained by Horst Lenk.

Table of Contents Entry:

The electronic structure of the vanadate cofactor in the peroxo-form is investigated for QM/MM models of VCPO and VBPO via critical comparison of both NMR parameters and UV-vis electronic transitions. Theoretical ^{51}V chemical shifts for the peroxo forms of VCPO and VBPO show only minor differences in the isotropic $\delta(^{51}\text{V})$ value, and somewhat more pronounced changes in the tensor values of both enzymes. When experimental solid-state NMR data become available, selection of the best model(s) should be possible, which would furnish insights into structural details (protonation state, H-bond network) of these enzymes at a key intermediate stage of the catalytic cycle.

Keywords: Haloperoxidases, QM/MM, Anisotropic chemical shifts, DFT.

Graphical Abstract:



References

1. Crans, D. C.; Smee, J. J.; Graidamauskas, E.; Yang, L. *Chem. Rev.* **2004**, *104*, 849-902.
2. Thompson, K. H.; McNeill, J. H.; Orvig, C. *Chem. Rev.* **1999**, *99*, 2561-2571.
3. Butler, A. *Coord. Chem. Rev.* **1999**, *187*, 17-35.
4. Pecoraro, V.; Slebodnick, C.; Hamstra, B.; in: Crans, D. C.; Tracey, A. (Eds.); Vanadium compounds: Chemistry Biochemistry and Therapeutic Applications, ACS Symposium Series 1998 Chapter 12, 711.
5. Ligtenbarg, A. G. J.; Hage, R.; Feringa, B. L. *Coord. Chem. Rev.* **2003**, *237*, 89-101.
6. Van Schijndel, J. W. P. M.; Vollenbroek, E. G. M.; Wever, R. *Biochem. Biophys. Acta.* **1993**, *1161*, 249.
7. R. Everett, A. Butler, *Inorg. Chem.* **1989**, *28*, 393-395.
8. Messerschmidt, A.; Prade, L.; Wever, R. *J. Biol. Chem.* **1997**, *378*, 309-315.
9. Renirie, R.; Hemrika, W.; Wever, R. *J. Biol. Chem.* **2000**, *275*, 11650.
10. Zampella, G.; Fantucci, P.; Pecoraro, V. L.; Gioia, L. D.; *Inorg. Chem.* **2006**, *45*, 7133-7143.
11. De Boer, E.; Tromp, M. G. M.; Plat, H.; Krenn, G. E.; Wever, R. *Biochim. Biophys. Acta.* **1986**, *872*, 104-115.
12. Colpas, G. J.; Hamstra, B. J.; Kampf, J. W.; Pecoraro, V. L. *J. Am. Chem. Soc.* **1996**, *118*, 3469-3478.
13. Zampella, G.; Fantucci, P.; Pecoraro, V. L.; Gioia, L. D. *J. Am. Chem. Soc.* **2005**, *127*, 953-960.
14. Hamstra, B. J.; Colpas, G. J.; Pecoraro, V. L. *Inorg. Chem.* **1998**, *37*, 949-955.
15. Colpas, G. J.; Hamstra, B. J.; Kampf, J. W.; Pecoraro, V. L. *J. Am. Chem. Soc.* **1996**, *118*, 3469-3478.
16. Hemrika, W.; Renirie, R.; Macedo-Riberio, S.; Messerschmidt, A.; Wever, R. *J. Biol. Chem.* **1999**, *274*, 23820-23827.
17. Butler, A.; Eckert, H. *J. Am. Chem. Soc.* **1989**, *111*, 2802-2809.
18. Rehder, D.; Casny, M.; Grosse, R. *Magn. Reson. Chem.* **2004**, *42*, 745-749.
19. Pooransingh, N.; Pomerantseva, E.; Ebel, M.; Jantzen, S.; Rehder, D.; Polenova, T. *Inorg. Chem.* **2003**, *42*, 1256-1266.

20. Pooransingh-Margolis, N.; Renirie, R.; Hasan, Z.; Wever, R.; Vega, A. J.; Polenova, T. *J. Am. Chem. Soc.* **2006**, *128*, 5190-5208.
21. Pooransingh-Margolis, N. **2005**, PhD Thesis, University of Delaware.
22. Waller, M. P.; Bühl, M.; Geethalakshmi K.R.; Wang, D.; Thiel, W. *Chem. Eur. J.* **2007**, *13*, 4723-4732.
23. Waller, M. P.; Geethalakshmi K. R.; Bühl, M. *J. Phys.Chem.B.* **2008**, *112*, 5813-5823.
24. Zampella, G.; Kravitz, J. Y.; Webster C. E.; Fantucci, P.; Hall, M. B.; Carlson H. A.; Pecoraro, V.L.; De Gioia, L. *Inorg. Chem.* **2004**, *43*, 4127-4136.
25. Bangesh, M.; Plass, W. *J. Mol. Struct. (Theochem)* **2005**, *725*, 163-175.
26. Kravitz, J. Y.; Pecoraro, V. L.; Carlson, H. A. *J. Chem, Theory Comput.* **2005**, *1*, 1265-1274.
27. Zhang, Y.; Gascon, J. A. *J. Inorg. Biochem.* **2008**, *102*, 1684–1690.
28. Raugei, S.; Carloni, P. *J. Phys. Chem. B* **2006**, *110*, 3747-3758.
29. www.rcsb.org/pdb/
30. Li, H.; Robertson, A. D.; Jensen, J. H. *Proteins* **2005**, *61*, 704-721.
31. a) MacKerell, Jr. A. D.; Bashford, D.; Bellott, M.; Dunbrack, Jr., R. L.; Evanseck, J. D.; Field, M. J.; Fischer, S.; Gao, J.; Guo, H.; Ha, S.; Joseph-McCarthy, D.; Kuchnir, L.; Kuczera, K.; Lau, F. T. K.; Mattos, C.; Michnick, S.; Ngo, T.; Nguyen, D. T.; Prodhom, B.; Reiher, III, W. E.; Roux, B.; Schlenkrich, M.; Smith, J. C.; Stote, R.; Straub, J.; Watanabe, M.; Wiórkiewicz-Kuczera, J.; Yin, D.; Karplus, M. *J. Phys. Chem. B* **1998**, *102*, 3586-3616; b) MacKerell, Jr., A. D.; Feig, M.; Brooks III, C. L. *J. Comp. Chem.* **2004**, *25*, 1400-1415.
32. Klähn, M.; Braun-Sand, S.; Rosta, E.; Warshel, A. *J. Phys. Chem. B* **2005**, *109*, 15645-1650.
33. Sherwood, P.; de Vries, A. H.; Guest, M. F.; Schreckenbach, G.; Catlow, C. R. A.; French, S. A.; Sokol, A. A.; Bromley, S. T.; Thiel, W.; Turner, A. J.; Billeter, S.; Terstegen, F.; Thiel, S.; Kendrick, J.; Rogers, S. C.; Casci, J.; Watson, M.; King, F.; Karlsen, E.; Sjøvoll, M.; Fahmi, A.; Schäfer, A.; Lennartz, Ch. *J. Mol. Struct. (Theochem)* **2003**, *632*, 1-28.
34. Ahlrichs, R.; Bär, M.; Häser, M.; Horn, H.; Kölmel, C. *Chem. Phys. Lett.* **1989**, *162*, 165–169.

35. a) Becke, A. D. *Phys. Rev. A* **1988**, *38*, 3098-3100. b) Perdew, J. P. *Phys Rev. B* **1986**, *33*, 8822-8824. c) Perdew, J. P. *Phys Rev. B* **1986**, *34*, 7406.
36. a) Wachters, A. J. H. *J. Chem. Phys.* **1970**, *52*, 1033-1036. b) Hay, P. J. *J. Chem. Phys.* **1977**, *66*, 4377-4384.
37. Hehre, W. J.; Ditchfield, R.; Pople, J. A. *J. Chem. Phys.* **1972**, *56*, 2257-2261.
b) P. C. Hariharan, J. A. Pople, *Theor. Chim. Acta*, **1973**, *28*, 213-222.
38. Eichkorn, K.; Weigend, F.; Treutler, O.; Ahlrichs, R.; *Theor. Chem. Acc.* **1997**, *97*, 119-124.
39. Smith, W.; Forester, T. *J. Molec. Graphics*, **1996**, *14*, 136.
40. a) MacKerell, Jr. A. D.; Bashford, D.; Bellott, M.; Dunbrack, Jr., R. L.; Evanseck, J. D.; Field, M. J.; Fischer, S.; Gao, J.; Guo, H.; Ha, S.; Joseph-McCarthy, D.; Kuchnir, L.; Kuczera, K.; Lau, F. T. K.; Mattos, C.; Michnick, S.; Ngo, T.; Nguyen, D. T.; Prodhom, B.; Reiher, III, W. E.; Roux, B.; Schlenkrich, M.; Smith, J. C.; Stote, R.; Straub, J.; Watanabe, M.; Wiórkiewicz-Kuczera, J.; Yin, D.; Karplus, M. *J. Phys. Chem. B* **1998**, *102*, 3586-3616; b) MacKerell, Jr., A. D.; Feig, M.; Brooks III, C. L. *J. Comp. Chem.* **2004**, *25*, 1400-1415.
41. Corresponding to model B in: Bakowies, D.; Thiel, W. *J. Phys. Chem.* **1996**, *100*, 10580-10594.
42. Reed, A.; Weinstock, R.; Weinhold, F. *J. Chem. Phys.* **1985**, *83*, 735-746.
43. Gaussian 03, Revision D.01, M. J. Frisch, G. W. Trucks, H. B. Schlegel, G. E. Scuseria, M. A. Robb, J. R. Cheeseman, J. A. Montgomery, Jr., T. Vreven, K. N. Kudin, J. C. Burant, J. M. Millam, S. S. Iyengar, J. Tomasi, V. Barone, B. Mennucci, M. Cossi, G. Scalmani, N. Rega, G. A. Petersson, H. Nakatsuji, M. Hada, M. Ehara, K. Toyota, R. Fukuda, J. Hasegawa, M. Ishida, T. Nakajima, Y. Honda, O. Kitao, H. Nakai, M. Klene, X. Li, J. E. Knox, H. P. Hratchian, J. B. Cross, V. Bakken, C. Adamo, J. Jaramillo, R. Gomperts, R. E. Stratmann, O. Yazyev, A. J. Austin, R. Cammi, C. Pomelli, J. W. Ochterski, P. Y. Ayala, K. Morokuma, G. A. Voth, P. Salvador, J. J. Dannenberg, V. G. Zakrzewski, S. Dapprich, A. D. Daniels, M. C. Strain, O. Farkas, D. K. Malick, A. D. Rabuck, K. Raghavachari, J. B. Foresman, J. V. Ortiz, Q. Cui, A. G. Baboul, S. Clifford, J. Cioslowski, B. B. Stefanov, G. Liu, A. Liashenko, P. Piskorz, I. Komaromi, R. L. Martin, D. J. Fox, T. Keith, M. A. Al-Laham, C. Y. Peng, A.

- Nanayakkara, M. Challacombe, P. M. W. Gill, B. Johnson, W. Chen, M. W. Wong, C. Gonzalez, J. A. Pople, Gaussian, Inc., Wallingford CT, **2004**.
44. a) Becke, A. D.; *J. Chem. Phys.* **1996**, *98*, 5648-5642. b) Lee, W.; Yang, R.; Parr, G. *Phys. Rev. B* **1988**, *37*, 785-789.
45. Clark, T.; Chandrasekhar, J.; Spitznagel, G.; Schleyer, P. *J. Comput. Chem.* **1983**, *4*, 294-301.
46. a) U. Haeberlen, In *Advances in Magnetic Resonance*; Suppl. 1; J. S. Waugh, Ed.; Academic Press: New York, **1976**. b) M. Mehring, *Principles of High Resolution NMR in Solids*, 2nd. ed.; Springer Verlag: Berlin, **1983**. c) H. W. Spiess, In *NMR Basic Principles and Progress*; P. Diehl, E. Fluck, R. Kosfeld, Eds.; Springer Verlag, Berlin, **1978**, Vol. 15.
47. Bak, M.; Rasmussen, J. T.; Nielsen, B. *J. Magn. Reson.* **2000**, *147*, 296-330 .
48. Andersson, I.; Angus-Dunne, S.; Howarth, O.; Pettersson, L. *J. Inorg. Biochem.* **2000**, *80*, 51-58.
49. Weyand, M.; Hecht, H-J.; Kiess, M.; Liaud, M.F.; Vitler, H.; Schomburg, D. *J. Mol. Biol.* **1999**, *293*, 595-611.
50. Tanaka, N.; Hasan, Z.; Wever, R. *Inorg. Chim. Acta*, **2003**, *356*, 288-296.
51. For instance, the presence of a single water molecule in the active site can affect activation barriers significantly: Altun, A.; Guallar, V.; Friesner, R. A.; Shaik, S.; Thiel, W. *J. Am. Chem. Soc.* **2006**, *128*, 3924-3925.
52. I.e. VCPO-D14, -D34, and -T144 with $\delta(^{51}\text{V}) = -624, -605, \text{ and } -592$ ppm, respectively, for the native form, and *p*-VBPO-Z and *p*-VBPO-S1 for the peroxo form.
53. a) Bühl, M.; Parrinello, M. *Chem. Eur. J.* **2001**, *7*, 4487-4494; b) Bühl, M.; Mauschick, F. T.; Schurhammer, R., in: *High Performance Computing in Science and Engineering, Munich 2002*, Wagner, S.; Hanke, W.; Bode, A.; Durst F. (Eds.), Springer Verlag, Berlin, 2003, pp.189-199.
54. See e.g. Dreuw, A.; Head-Gordon, M. *J. Am. Chem. Soc.* **2004**, *126*, 4007
55. For some recent examples see: a) Adams, C. J.; Fey, N.; Harrison, Z. A.; Sazanovich, I. V.; Towrie, M.; Weinstein. J. A. *Inorg. Chem.* **2008**, *47*, 8242–8257. b) Lage, M. L.; Fernandez, I.; Mancheno, M. J.; Sierra, M. A.; *Inorg. Chem.* **2008**, *47*, 5253–5258.

56. Renirie, R.; Hemrika, W.; Piersma, S.; Wever, R. *Biochemistry* **2000**, *39*, 1133-1141.
57. Tromp, M. G. M.; Olafsson, G.; Krenn, B. E.; Wever, R. *Biochem. Biophys. Acta.* **1990**, *1040*, 192-198.
58. For consistency with the QM/MM computations for the enzymes, an analogous setup has been employed for this system, namely MD equilibration of a hydrated cluster (vanadate and 18,000 water molecules), followed by BP86/AE1 / TIP3P optimization for six snapshots and averaging of the TD-B3LYP/AE1(+) data computed for these minima (including the MM charges - if these are omitted, the computed λ_{\max} value increases by ca. 10 nm),